

Effects of (i)a-Si:H deposition temperature on high-efficiency silicon heterojunction solar cells

Yifeng Zhao¹  | Paul Procel^{1,2}  | Arno Smets¹ | Luana Mazzarella¹ |
Can Han¹  | Guangtao Yang¹ | Liqi Cao¹  | Zhirong Yao¹ |
Arthur Weeber^{1,3} | Miro Zeman¹ | Olindo Isabella¹

¹Photovoltaic Materials and Devices Group, Delft University of Technology, Delft, The Netherlands

²Institute of Micro and Nanoelectronics, San Francisco de Quito University, Quito, Ecuador

³TNO Energy Transition, Solar Energy, Petten, The Netherlands

Correspondence

Yifeng Zhao, Photovoltaic Materials and Devices Group, Delft University of Technology, Delft, The Netherlands.

Email: y.zhao-4@tudelft.nl

Funding information

NWO Joint Solar Program III, Grant/Award Number: 680-91-011

Abstract

Excellent surface passivation induced by (i)a-Si:H is critical to achieve high-efficiency silicon heterojunction (SHJ) solar cells. This is key for conventional single-junction cell applications but also for bottom cell application in tandem devices. In this study, we investigated the effects of (i)a-Si:H deposition temperature on passivation quality and SHJ solar cell performance. At the lower end of temperatures ranging from 140°C to 200°C, it was observed with Fourier-transform infrared spectroscopy (FTIR) that (i)a-Si:H films are less dense, thus hindering their surface passivation capabilities. However, with additional hydrogen plasma treatments (HPTs), those (i)a-Si:H layers deposited at lower temperatures exhibited significant improvements and better passivation qualities than their counterparts deposited at higher temperatures. On the other hand, even though we observed the highest V_{OC} s for cells with (i)a-Si:H deposited at the lowest temperature (140°C), the related FF s are poorer as compared to their higher temperature counterparts. The optimum trade-off between V_{OC} and FF for the SHJ cells was found with temperatures ranging from 160°C to 180°C, which delivered independently certified efficiencies of 23.71%. With a further improved p -layer that enables a FF of 83.3%, an efficiency of 24.18% was achieved. Thus, our study reveals two critical requirements for optimizing the (i)a-Si:H layers in high-efficiency SHJ solar cells: (i) excellent surface passivation quality to reduce losses induced by interface recombination and simultaneously (ii) less-defective (i)a-Si:H bulk to not disrupt the charge carrier collections.

KEYWORDS

FTIR, intrinsic amorphous silicon, passivation, silicon heterojunction solar cells

1 | INTRODUCTION

Front/back-contacted silicon heterojunction (FBC-SHJ) solar cells have achieved a remarkable efficiency of 26.50%.¹ Application of SHJ cells in tandem devices resulted in record two-terminal

(2T) perovskite-silicon tandem efficiencies of 30.93% and 31.25% with a front-flat and a front-textured surfaces, respectively.² One of the crucial ingredients that enable such high efficiencies is the excellent open-circuit voltage (V_{OC}) above 750 mV of SHJ cells, which is mainly provided by a few nanometer thick hydrogenated intrinsic

This is an open access article under the terms of the [Creative Commons Attribution](https://creativecommons.org/licenses/by/4.0/) License, which permits use, distribution and reproduction in any medium, provided the original work is properly cited.

© 2022 The Authors. Progress in Photovoltaics: Research and Applications published by John Wiley & Sons Ltd.

amorphous silicon (*i*)a-Si:H film. Therefore, careful optimization of the (*i*)a-Si:H deposition conditions is essential to enable high-efficiency SHJ solar cells and their application in tandem solar cells. In general, optimized (*i*)a-Si:H should be deposited with dense bulk quality while suppressing the detrimental epitaxial growth at the c-Si/(*i*)a-Si:H interface.³ Approaches have been proposed to enhance the surface passivation qualities of (*i*)a-Si:H layer, such as using hydrogen-diluted SiH₄,^{4–7} pre- or post-hydrogen plasma treatment (HPT),^{8–15} (*i*)a-Si:H bilayer stacks^{5,16–22} and post-annealing.^{3,23,24} Subsequent overlaying of doped layers and transparent conductive oxide (TCO) on the (*i*)a-Si:H layers also impose challenges on preserving their passivation qualities of the c-Si surface.^{25,26}

Apart from the necessity of having excellent passivation induced by (*i*)a-Si:H, SHJ solar cells should also feature efficient charge carrier transport from c-Si bulk to the TCO. Notwithstanding the importance of tuning the electrical properties of doped layers and TCO layers for achieving efficient selective transport of charge carriers,²⁷ different bulk qualities of (*i*)a-Si:H may also impact differently the charge carrier collections.^{17,28,29} Interestingly, either (*i*)a-Si:H monolayers or bilayers that feature an underdense (*i*)a-Si:H close to c-Si surface showed better passivation qualities as compared to their dense counterparts. On the other hand, those underdense films may also cause increased series resistance of solar cells.^{17,28,29} Therefore, the revealed trade-off between passivation and carrier collections with respect to (*i*)a-Si:H requires attentive optimization efforts.

Aiming at further understanding and exploring the potential of the excellent passivation induced by (*i*)a-Si:H, in this study, we analyzed in detail the optical and microstructural properties of (*i*)a-Si:H layers deposited under various temperatures between 140°C and 200°C, and applied them to SHJ solar cells. Besides, the effects of our optimized HPT and very-high-frequency treatment (VHF treatment)¹⁵ on (*i*)a-Si:H passivation quality are also studied. We addressed the microstructural evolution of (*i*)a-Si:H layers under various conditions via Fourier-transform infrared (FTIR) spectroscopy measurements. Accordingly, those microstructural properties of (*i*)a-Si:H layers provided possible explanations for their passivation capabilities and their impacts on solar cells.

2 | EXPERIMENTAL DETAILS

In this study, we deposited thin-film silicon layers with a multi-chamber plasma-enhanced chemical vapor deposition (PECVD) tool (Elettrovava S.p.A.). The PECVD operates at either radio-frequency

(RF, 13.56 MHz) or very-high frequency (VHF, 40.68 MHz). We adjusted the PECVD deposition conditions to obtain various (*i*)a-Si:H layers as listed in Table 1. Additionally, we also applied the previously optimized HPT and VHF treatment (thereafter simplified as HPTs) on (*i*)a-Si:H layers, and their main PECVD parameters are provided in Table 1. The VHF treatment consists of highly H-diluted SiH₄ plasma, which mainly modifies the microstructure of (*i*)a-Si:H layers rather than depositing (*i*)nc-Si:H, as no change in the thickness of (*i*)a-Si:H was detected via spectroscopic ellipsometry (SE) after 6 min of this VHF treatment.¹⁵ The detailed deposition conditions of doped layers can be found in our previous studies.^{30,31}

Different glass and *n*-type c-Si samples, as schematically illustrated in Figure 1, were prepared to evaluate the effects of the deposition temperature and HPTs on (*i*)a-Si:H layers and their further applications in SHJ solar cells. The abbreviations, stack descriptions and temperatures for layers and HPTs investigated in this study are given in Table 2. Specifically, SE (M-2000DI system, J.A. Woollam Co., Inc.) was used to extract the optical bandgap (E_{04}) and refractive index (n at the wavelength of 632 nm) of (*i*)a-Si:H layers deposited on glass substrates (Corning Eagle XG). FTIR spectroscopy (Thermo Fisher Nicolet 5700 in the transmittance mode) was used to analyze the evolution of the hydrogen bonding configurations and the microstructure of (*i*)a-Si:H layers under various conditions. Effective lifetimes (τ_{eff}) of the minority carriers in symmetrical passivation samples were measured with Sinton WCT-120 with either transient photoconductance decay mode or quasi-steady-state photoconductance mode. Note, the deposition conditions of HPT for the *p*-side, as listed in Table 1, were used as the representative HPT for both FTIR and symmetrical (*i*)a-Si:H passivation samples. The HPTs etches around 2 nm of the (*i*)a-Si:H bilayer on each side of the c-Si wafer.

For FTIR characterizations, we used single-side-flat Siegrt Czochralski (CZ) <100> c-Si wafers with thicknesses of 480 ± 20 μm and resistivities of 15 ± 5 $\Omega\cdot\text{cm}$. For symmetrical passivation tests and solar cell fabrications, we used (*n*)-type Topsil float-zone (FZ) <100> c-Si wafers, which are 280 ± 20 μm -thick with resistivities of 3 ± 2 $\Omega\cdot\text{cm}$. Prior to PECVD depositions, both types of wafers were textured to obtain a random distribution of pyramids in diluted tetramethylammonium hydroxide (TMAH) solution with ALKA-TEX as additives.³² Subsequently, they were sequentially cleaned by room-temperature 99% nitric acid (HNO₃), 110°C 69.5% HNO₃, and lastly 0.55% HF. During PECVD depositions for solar cells (precursors), we firstly deposited layer stacks for the *n*-side. Then with a short vacuum break, the wafers were flipped for subsequent depositions of the layer stacks for the *p*-side. After PECVD, RF magnetron sputtering

TABLE 1 PECVD deposition parameters of different (*i*)a-Si:H layers, HPT and VHF treatment

	(<i>i</i>)a-Si:H-1	(<i>i</i>)a-Si:H-2	HPT	VHF treatment
$f[\text{H}_2]/f[\text{SiH}_4]$ (sccm/sccm)	0/40	30/10	200/0	120/1.2
Pressure (mbar)	0.7	1.4	2.7 (for <i>n</i> -side)/2.2 (for <i>p</i> -side)	4.0
Power density (mW/cm ²)	20.8	20.8	62.5	90.3
Temperature (°C)	140–200	140–200	180	180

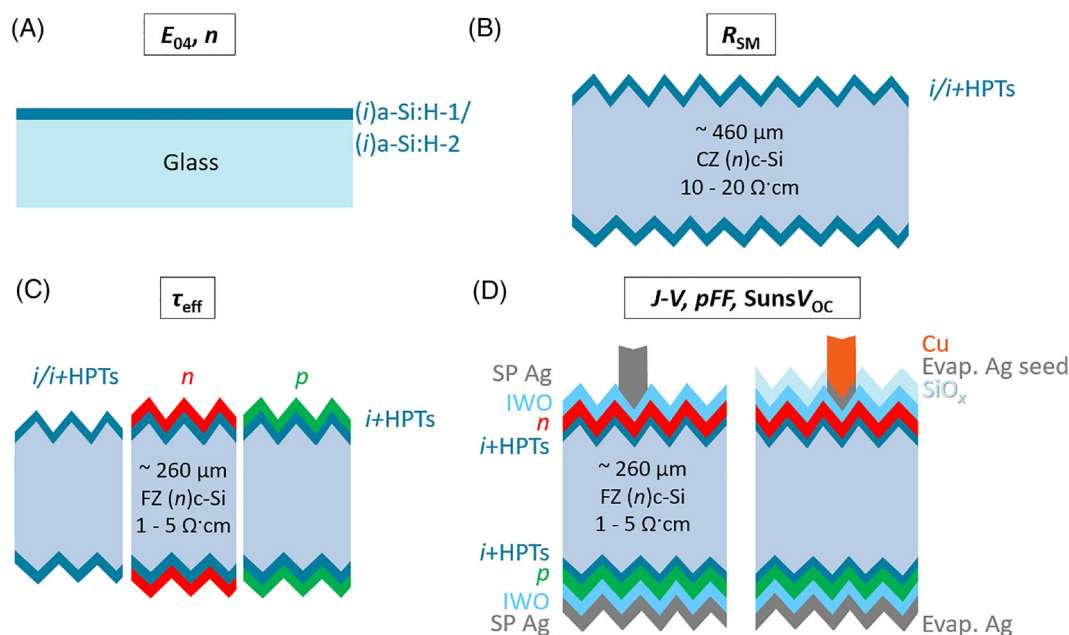


FIGURE 1 Schematic sketches of sample structures for (A) extracting E_{04} and n , (B) FTIR measurements, (C) obtaining τ_{eff} , and (D) rear junction FBC-SHJ solar cells fabricated in this study

TABLE 2 Abbreviations, stack descriptions and deposition temperatures for layers and HPTs forming the SHJ solar cells

Abbreviations	Descriptions	Temperature ($^{\circ}\text{C}$)
i	1 nm (i)a-Si:H-1 + 7 or 8 nm (i)a-Si:H-2*	140–200
HPTs	HPT + VHF treatment	180
n	3 nm (n)nc-Si:H** + 2 nm (n)a-Si:H	180
p	5 nm (p)nc-SiO _x :H** + 16 nm (p)nc-Si:H	180

*7 nm and 8 nm (i)a-Si:H-2 for n - and p -layers, respectively.

**With such thin thicknesses, both the 3 nm (n)nc-Si:H³¹ and 5 nm (p)nc-SiO_x:H (not shown) are amorphous-phase dominant and yet to develop well-defined nanocrystals.

(Polyteknik AS) was used for depositing room-temperature tungsten-doped indium oxide (IWO).³³ Then, solar cell precursors with both-sides as-deposited IWO were annealed in air at 180 $^{\circ}\text{C}$ for 5 min. Eventually, solar cells were fabricated with screen-printed (SP) Ag contacts on both sides with a curing step in the air at 170 $^{\circ}\text{C}$ for 40 min. Alternatively, we also applied our optimized room-temperature copper-plating metallization approach to form front metal grids while using 500-nm-thick thermally evaporated Ag for forming the rear contact.³⁴ To further improve the anti-reflection effect of the completed solar cells, a 100-nm-thick SiO_x was optionally deposited via e-beam evaporation on the front side of the devices.^{33,35} Solar cells fabricated in this study have a designated area of 3.92 cm².

Along the fabrication process of solar cells, we also measured the τ_{eff} of cell precursors before and after IWO sputtering with Sinton

WCT-120. The current-voltage (I - V) characteristics of solar cells were evaluated with a AAA class Wacom WSX-90S-L2 solar simulator under standard-test-conditions (STC). To extract the series resistance of solar cells,³⁶ we obtained the pseudo- FF (pFF) from Sinton Suns-V_{OC}-150 Illumination-Voltage Tester. The independently certified I - V parameters were obtained from the CalTeC of the Institute for Solar Energy Research Hamelin (ISFH), Germany.

Based on FTIR measurements, we extracted the microstructure factor (R_{SM}) that is defined for Si-H stretching modes (SM) of (i)a-Si:H layers as³⁷

$$R_{\text{SM}} = I_{\text{HSM}} / (I_{\text{LSM}} + I_{\text{HSM}}) \quad (1)$$

where LSM and HSM stand for low-frequency SM (at 1980–2010 cm^{−1}) and high-frequency SM (at 2070–2100 cm^{−1}),^{38–40} respectively, and I is the integrated absorbance³⁹:

$$I = \int \left(\frac{\alpha^*}{\omega} \right) d\omega \quad (2)$$

$\alpha^*(\omega)$ is the effective absorption coefficient at ω and it is proportional to $-\ln(T(\omega))/t$ if $\alpha^*(\omega)t \ll 1$. The $T(\omega)$ is the transmittance obtained from the FTIR measurements, and t is the effective thickness of the film, which counts for films deposited on both sides. Traditionally, FTIR analyses are performed on films deposited on flat c-Si substrates; however, in this work, the textured c-Si substrates as integrated in the SHJ solar cell devices are used. For simplicity, the effective film thickness on each side is assumed to be 1.7 times of film thickness that is perpendicular to the pyramid facet. Note, in reality, the effective film thickness is larger than this assumption due to

effects induced by the use of textured samples, such as reduced reflection thus resulting in enhanced light incorporation and prolonged optical path. Nevertheless, the relative comparisons among samples are still valid with this assumption.

3 | RESULTS AND DISCUSSIONS

3.1 | Temperature effects on (i)a-Si:H monolayers' optical properties

To understand the effects of (i)a-Si:H deposition temperature on their optical properties, we deposited the two types of (i)a-Si:H (~ 20 nm) described in Table 1 on glass substrates (see Figure 1A). Figure 2 presents the extracted E_{04} and n at the wavelength of 632 nm of (i)a-Si:H layers via SE.

As shown in Figure 2, for the temperature range investigated (140°C to 200°C), we observed monotonic decrements of the E_{04} and increments of the n with higher deposition temperatures for both (i)a-Si:H layers. A higher E_{04} often indicates a higher hydrogen content in the (i)a-Si:H layer⁴¹; that is, both (i)a-Si:H layers deposited under lower temperatures are likely to be more H-rich than the higher temperature counterparts. Besides, we ascribe the lower n of (i)a-Si:H deposited under lower temperatures to the relatively lower film densities. Those observations agree well with previous studies.^{4,21} Therefore, based on both E_{04} and n , the films seem to become denser but they incorporate less hydrogen by increasing the deposition temperature of the (i)a-Si:H layers.

3.2 | Temperature and HPTs effects on (i)a-Si:H layers' microstructural properties

To prevent possible epitaxial growth of the highly H-diluted (i)a-Si:H-2 when deposited directly on c-Si, we followed the bilayer approach that improved the passivation quality and efficiency of our SHJ solar cells (see Table S2). The bilayer consists of a 1-nm-thick (i)a-Si:H-1 layer without additional H-dilution⁴² that acts as a buffer for the subsequent deposition of the highly H-diluted (i)a-Si:H-2 layer. To

gain more insights into the (i)a-Si:H layers with cell-relevant growth conditions, it is worth noting that we used double-side-textured substrates with the same (i)a-Si:H thicknesses as used in solar cells for FTIR measurements. The microstructure and hydrogen-bonding configuration of bilayer stacks deposited under various temperatures were assessed by FTIR on dedicated samples as sketched in Figure 1B. Besides, we also evaluated the effects of HPTs on the microstructural properties of the bilayer stacks. The infrared spectra of different (i)a-Si:H bilayers are presented in Figure 3. The infrared spectra of single (i)a-Si:H layers deposited at 160°C were given in Figure S2.

As seen in Figure 3A, detailed information from the peaks around the wavenumber of 2000 , 880 and 640 cm^{-1} can be extracted to characterize our (i)a-Si:H bilayers. Firstly, the peak around 2000 cm^{-1} can be typically deconvoluted into two Gaussian distributions for a-Si:H, which are related to the Si-H LSM and HSM as visible in Figure 3A. It has been demonstrated that the LSM is attributed to monohydrides in small volume deficiencies,^{43,44} whereas HSM is assigned to mainly the monohydrides and some polyhydrides at internal surfaces of larger volume deficiencies like nano-sized voids.^{39,43,44} As a result of the different Si-H bonding nature of LSM and HSM, a higher fraction of HSM, thus a higher R_{SM} (defined previously in the experimental details) indicates a less compact or void-rich film. For simplicity, as for (i)a-Si:H bilayers without HPTs, peaks centered at 2000 and 2090 cm^{-1} are assigned to LSM and HSM, respectively.

As seen around the SM region in Figure 3A, for (i)a-Si:H bilayers without HPTs, instead of the I_{LSM} that only slightly vary with deposition temperatures, we observed more significant monotonic decrements of I_{HSM} with increasing deposition temperatures. As a result, (i)a-Si:H bilayers deposited at lower temperatures featured larger R_{SM} values as compared to the higher temperature counterparts. In other words, (i)a-Si:H bilayers are more void-rich as they contain silicon hydrides at internal void surfaces when deposited at lower temperatures, which could result in higher hydrogen content in the films as well. This finding is in good agreement with the optical properties we reported in Figure 2 as well as with previous studies.^{4,21,45–47} Moreover, at the wavenumber of around 880 cm^{-1} , which reflects the bending modes (BM) of polyhydrides,⁴³ we observed peaks with gradually decreased absorption strength for layers with higher deposition temperatures. This also suggests the relatively higher fractions of polyhydrides for films deposited under lower temperatures.

Similar to (i)a-Si:H bilayers without HPTs, the R_{SM} for the (i)a-Si:H bilayers with HPTs is also higher for films deposited at lower temperatures, although the R_{SM} differences between different temperatures are less prominent (see Figure 3A). The overall increased R_{SM} indicates that H-incorporation through our HPTs reconfigures the Si-H bonding configurations and favors the formation of the HSM components in the (i)a-Si:H bilayers. The formation of polyhydrides that contribute to the HSM after HPTs is also reflected in the observed peaks that represent polyhydrides BM as presented in Figure 3A. It is worth noting that we applied a slight shift of frequency from 2000 to 2010 cm^{-1} for the LSM to obtain better fittings to the raw data. This shift of frequency is a result of the reduced electrical screening of the Si-H

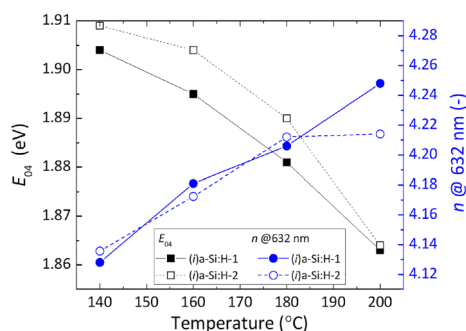


FIGURE 2 The E_{04} and n of (i)a-Si:H layers deposited at variable temperatures

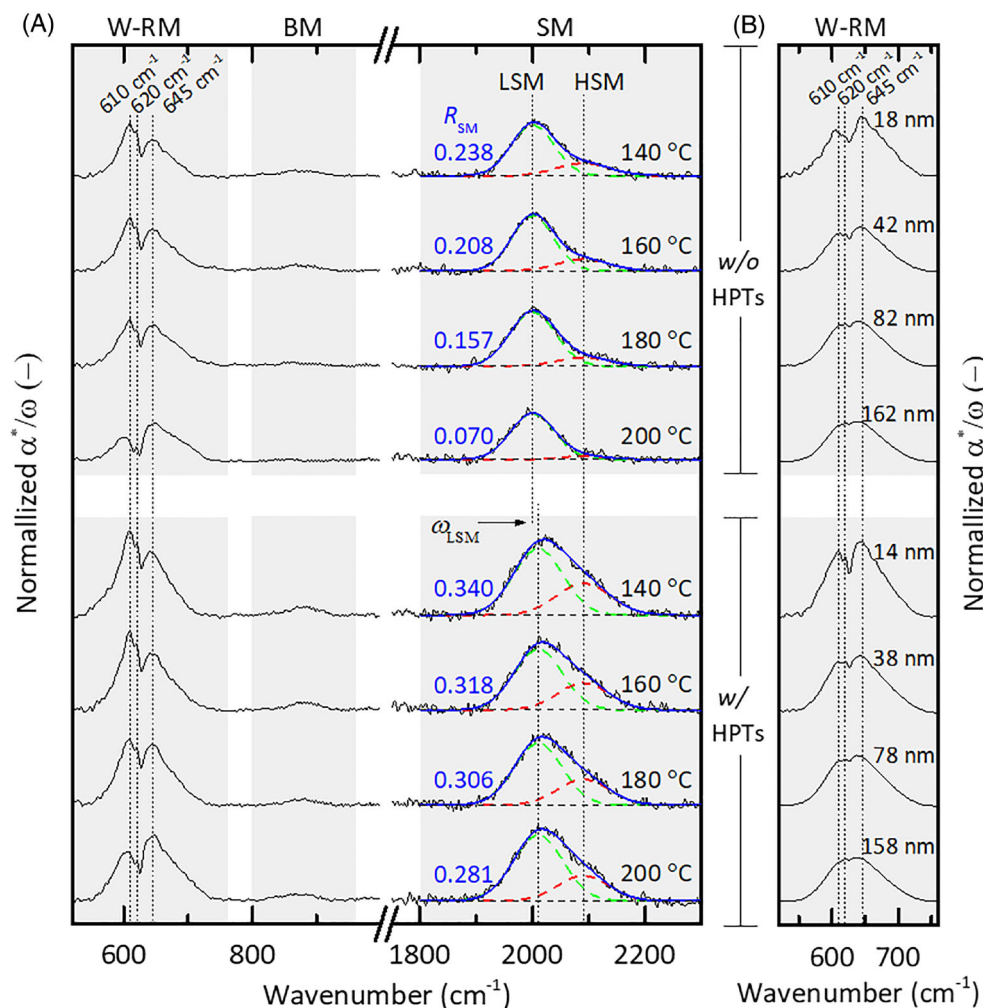


FIGURE 3 The infrared spectra of (i)a-Si:H bilayers deposited (A) at various temperatures with (w/) or without (w/o) HPTs; (B) with various thicknesses w/ or w/o HPTs. For part (A), the thickness of deposited layers before HPTs is in total 18 nm on both sides of the substrate. For part (B), those (i)a-Si:H bilayers consist of a 1-nm-thick (i)a-Si:H-1 layer with a (i)a-Si:H-2 layer featuring varied thickness, the deposition temperature was fixed at 160 °C and the indicated thickness numbers are total thickness on both sides of the wafer. The infrared spectra were normalized according to the thicknesses of (i) a-Si:H bilayers as discussed in experimental details. Those thicknesses are based on the deposition rates calculated from flat samples. In both parts, W-RM stands for Si-H wagging-rocking modes, BM refers to Si-H polyhydrides bending modes, SM represents Si-H stretching modes. In the SM region, the green and red dashed lines represent the fitted Gaussian function for LSM and HSM, respectively. The blue solid lines are the overall fittings. Note that the series of samples in Figure 3A were processed in different batches as compared to Figure 3B.

dipole vibrations by a less dense dielectric and additionally indicates the formation of more porous films after HPTs as discussed in the previous work.⁴⁸ Besides, we also noticed the overall improved absorption strength of the SM as compared to films without HPTs.¹⁵ This could be correlated to the following causes: (a) the HPTs incorporate significant amounts of additional H into the films⁴⁸; (b) as the (i)a-Si:H bilayers after HPTs are thinner, H-rich “interface” or “surface” layers will be more dominant (HSM) in reference to the “bulk” component (LSM),⁴⁹ and therefore featuring relatively higher volume deficiencies. Thus, the average dielectric constant will be lower and, as a consequence, the proportionality constant of the dipole oscillation is lower as well.⁵⁰ For a given hydrogen content, this lower proportionality constant will eventually result in enhanced absorption signals for layers with HPTs. Nevertheless, the latter cannot be the main contribution to the overall enhanced absorption signals, and HPTs indeed result in significant additional H-incorporation into the (i)a-Si:H bilayers. Overall, it is not straightforward to calculate absolute hydrogen concentration based on the proportionality constants provided in

previous study³⁹ because these “constants” may vary with layers’ thicknesses for very thin films, and with the textured morphology of our FTIR samples, which enables the prolonged optical path of infrared light inside the (i)a-Si:H bilayers as compared to typically used flat samples.

With respect to the Si-H wagging-rocking mode (W-RM), commonly one absorption peak centered at the wavenumber of 640 cm^{-1} is observed.^{39,51–53} Instead, it should be noticed that we observed at least three distinguishable peaks at around 610, 620 and 645 cm^{-1} (see Figure 3A). Although similar observations were reported in the literature for a-Si:H, only two peaks around 590 and 635 cm^{-1} were identified.^{38,54} To the best of our knowledge, here, we report for the first time at least three distinctive peaks around the W-RM for (i)a-Si:H. To further investigate the possible origin of this unexpected multi-peak characteristic, we carried out experiments with variable (i)a-Si:H bilayer thickness as shown in Figure 3B. Those (i)a-Si:H bilayers consist of a 1-nm-thick (i)a-Si:H-1 layer with a (i)a-Si:H-2 layer featuring varied thickness. Interestingly, with a thicker bilayer, we noticed a

progressively decreased absorption strength of the peak at around 610 cm^{-1} (see Figure 3B). Meanwhile, the signature of peaks at around 610 and 620 cm^{-1} became less distinguishable for thicker layers as they started to merge with the third absorption peak centered at around 645 cm^{-1} . This thickness-dependent characteristic suggests that the peak at around 610 cm^{-1} may be attributed to well-defined silicon-hydride wagging mode(s) that is (are) specific to the “surface” or “interface” nature between the (i)a-Si:H and c-Si surface, while peaks at around 645 cm^{-1} (also 620 cm^{-1}) may be ascribed to the “bulk” component as proposed in⁴⁹ (detailed discussions can be found in Figure S3). Unlike that of SM, due to the insufficiently distinctive assignments of absorption peaks around W-RM,^{38,43,51,55} it is not possible for us to deconvolute the observed W-RM absorption peaks. Still, several attempts for deconvoluting W-RM have been reported previously for investigating the phase transition from a-Si:H to $\mu\text{c-Si:H}$, in which a similar vibrational origin for peaks at 620 and 2100 cm^{-1} was proposed.^{56,57}

Nevertheless, for (i)a-Si:H bilayers without HPTs as shown in Figure 3A, we noticed that the absorption strength of mainly the peak at the wavenumber of 610 cm^{-1} decreases with increasing deposition temperatures, while the absorption strength of peaks at 620 and 645 cm^{-1} seemingly only slightly varied. That is, (i)a-Si:H bilayers deposited at higher temperatures feature reduced “surface” or “interface” components, thus resulting in a higher fraction of “bulk” components according to our speculations based on samples with varied thicknesses. It is known that the “surface” and “interface” part of the (i)a-Si:H are more void- and H-rich as compared to the “bulk” counterpart mainly due to their higher fraction of polyhydrides.^{49,58–60} Thus the variations of absorption strength around the W-RM may reflect a denser film with higher deposition temperatures. This finding agrees well with the observed lower R_{SM} with higher deposition

temperatures as seen from the SM (see Figure 3A). Further for (i)a-Si:H bilayers with HPTs, the same temperature-dependent trend was found. Similarly, we also observed systematically enhanced absorption strength of peaks after HPTs, which can be attributed to the same reasons as proposed for the SM. Overall, especially for layers with HPTs, those absorption peaks around W-RM seem to be more sensitive to varied deposition temperatures as compared to those around the SM. Thus, those peaks around W-RM might be capable of revealing more details about the changes in microstructure and Si-H bonding configurations in the film or the interface between c-Si and the film (see also the discussion in Figure S3). To understand more about these absorption peaks around the W-RM, more distinct assignments of specific Si-H vibrational modes around those wavenumbers would provide more insights.

To summarize, for layers with and without HPTs, a lower deposition temperature tends to result in more void-rich and H-rich (i)a-Si:H layers. The HPTs significantly incorporate additional H into the films and increase the large volume deficiencies of the films, and consequently, resulting in more hydrogenated surfaces in the (i)a-Si:H layers.

3.3 | Temperature effects on passivation quality for SHJ solar cells

We investigated the effects of (i)a-Si:H deposition temperature on the passivation qualities of the (i)a-Si:H layers and the effects of the additional HPTs on symmetrically coated c-Si wafers (see the schematic sketch in Figure 1C). Further, the passivation qualities of the (i)a-Si:H layers coated with doped contacts were also investigated. The τ_{eff} values of symmetrical samples are plotted in Figure 4A.

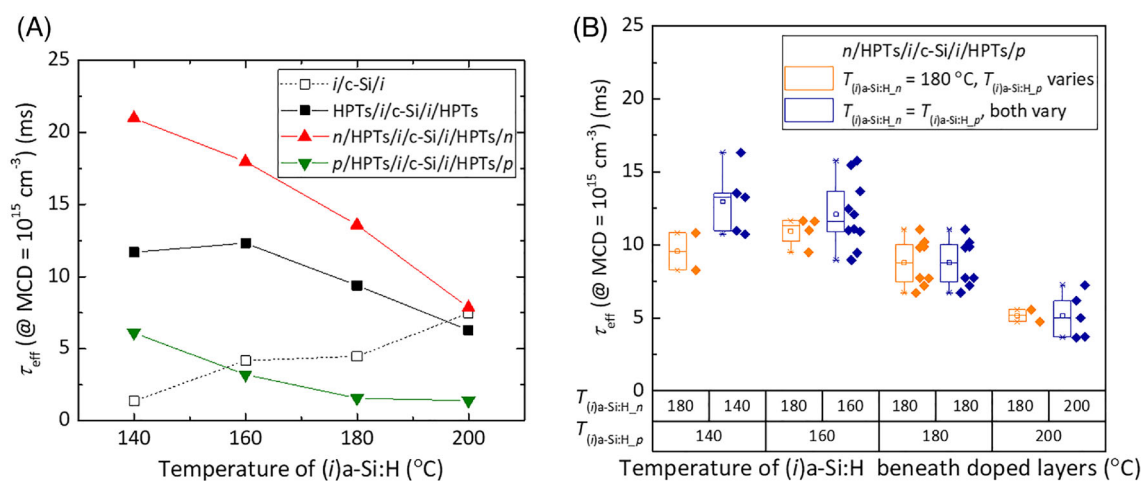


FIGURE 4 The τ_{eff} values of (A) symmetrical samples for individually checking passivation of different (i)a-Si:H layers under various temperatures and with doped layers, and (B) solar cell precursors without TCO with various deposition temperatures of (i)a-Si:H bilayers. In (A), lines are guides to the eye. Note in (B), $T_{(i)a-Si:H,n}$ and $T_{(i)a-Si:H,p}$ represent the deposition temperature of (i)a-Si:H layer beneath the n- and p-layers, respectively. The deposition temperatures of doped layers and HPTs were kept constant at 180°C as listed in Table 2. In part (B), for the samples that feature $T_{(i)a-Si:H,n} = T_{(i)a-Si:H,p} = 180^\circ\text{C}$, the box plot is duplicated for easier comparison in different temperature series.

As seen in Figure 4A, for passivation samples with only (i)a-Si:H bilayer (open symbols), higher deposition temperatures of (i)a-Si:H bilayers result in better passivation qualities. This could be attributed to the denser or less-defective (i)a-Si:H bilayers deposited at higher temperatures as confirmed by our FTIR measurements (see Figure 3A).⁴⁶ However, when additional HPTs were applied, the trend is reversed. For (i)a-Si:H bilayer deposited under 140°C (160°C) and treated with HPTs, the τ_{eff} was boosted from 1.4 ms (4.2 ms) to 11.7 ms (12.3 ms), while the passivation qualities with the additional HPTs showed fewer improvements and even degraded τ_{eff} with increasing deposition temperature of (i)a-Si:H bilayers to above 160°C. As known from the FTIR results shown in Figure 3A, the HPTs increase both the porosity and the hydrogen concentration of the (i)a-Si:H bilayer. In the meanwhile, HPTs could also create defects near the c-Si/(i)a-Si:H interface.⁶¹ We ascribe the observed better passivation qualities with (i)a-Si:H bilayer deposited under lower temperature conditions to (a) their initial highly porous microstructure, which is beneficial for more effectively preventing the possible detrimental epitaxial growth induced by highly H-diluted (i)a-Si:H-2; (b) protecting near-surface c-Si bulk from defect formations induced by H-radicals within HPTs²¹; (c) their higher concentrations of polyhydrides, which could be beneficial for further passivating the c-Si dangling bonds as they can act as H-reservoir for hydrogenations during the thermal processes⁴⁹; and (d) their more void-rich or defect-rich films that could promote easier H-diffusion to the c-Si/(i)a-Si:H interface.^{62–64} Lastly, with doped layers, we observed similar trends to that of the bilayer with HPTs. We found overall increments of the passivation qualities when *n*-layers were applied. It is worth noting that a τ_{eff} of nearly 21.0 ms was achieved with the (i)a-Si:H bilayer deposited at 140°C and coated with *n*-layers. Notwithstanding, we observed non-negligible degradations of τ_{eff} after the depositions of the *p*-layer that may require further passivation optimizations. Nevertheless, those degraded τ_{eff} values could be also ascribed to the over-annealing of the firstly deposited *i/p* stack during the deposition of the second *i/p* stack on the other side of the wafer.^{25,65}

Subsequently, solar cell precursors following the findings in Figure 4A were fabricated. The deposition temperatures of (i)a-Si:H bilayers underneath either only the *p*-layer or both doped layers were varied. The description of solar cell precursors and their τ_{eff} values are presented in Figure 4B. As expected, cell precursors that feature (i)a-Si:H bilayer with lower deposition temperatures exhibit better passivation qualities for both temperature series as shown in Figure 4B. Especially, a high τ_{eff} of 16.3 ms was achieved with the (i)a-Si:H bilayer deposition temperature fixed at 140°C for both doped layers. This good passivation is promising to achieve high-efficiency SHJ solar cells.

3.4 | Temperature effects on solar cells' J-V parameters

As (i)a-Si:H not only passivates the c-Si surface but should also contribute to the transport of charge carriers, different bulk qualities of (i)a-Si:H may impact the charge carrier collections differently. To this

end, we fabricated FBC-SHJ solar cells with screen-printed Ag contacts (sketched in Figure 1D) to evaluate the effects of (i)a-Si:H deposition temperature on devices' J-V parameters. The results are summarized in Figure 5. Note that the effects of HPTs on solar cells were discussed in our previous publications when optimizing either *n*- or *p*-type nc-Si:H-based contact stack with (i)a-Si:H deposited at 180°C.^{15,30,31} In those studies, we found that solar cell performances were improved after applying the HPTs mainly due to the H-rich and porous (i)a-Si:H layers formed after the HPTs (see Figure 3), where the H can largely suppress the surface recombination (see Figure 4A). Besides, the nucleation of overlaying doped nc-Si:H layers could also be promoted resulting in an enhancement of the selective transport of charge carriers.^{66–69}

For cells with a fixed (i)a-Si:H deposition temperature underneath the *n*-layer ($T_{(i)a-Si:H,n}$) (see Figure 5), we observed higher average V_{OC} values for cells with lower (i)a-Si:H deposition temperatures as expected from the trends discussed in Figure 4. However, the *FF* values of cells with (i)a-Si:H deposited at 140°C beneath *p*-layer ($T_{(i)a-Si:H,p} = 140^\circ\text{C}$) are averagely lower than those obtained for (i)a-Si:H deposited at higher temperatures. We ascribe this fact mainly to the more porous or defect-rich (i)a-Si:H bilayer deposited at 140°C as elucidated in Figure 3A. Besides, the rather wide distribution of *FF* for cells with $T_{(i)a-Si:H,p} = 140^\circ\text{C}$ could be attributed to the less microstructurally homogeneous films under such deposition conditions. The observation of those lower *FF* values is also supported by literature, where more defect-rich (i)a-Si:H deposited under lower temperature also increases the device series resistance²¹ (see also Figure S4). Besides, it was also discussed in the literature that void-rich (i)a-Si:H layers result in increased contact resistivity as those layers may feature unfavorable energetic position of defect states, the possible lower effective contact area on the c-Si surface, and likely the stronger effects on weakening the band bending induced by doped layers.²⁹ While cells with slightly less-defective (i)a-Si:H that was deposited at 160°C exhibited significantly improved *FF* to above 80% as compared to those with 140°C. Further, by increasing the deposition temperatures up to 200°C, solar cells showed saturated or slightly lower *FF*s, which are mainly due to the increased surface recombination as indicated by their lower V_{OC} values.^{28,70} Therefore, a trade-off between the passivation and carrier collections is revealed for varied $T_{(i)a-Si:H,p}$. Minor effects of (i)a-Si:H deposition temperature on J_{SC} were found (see also Figure S4).

Interestingly, by comparing solar cells with fixed $T_{(i)a-Si:H,p}$, higher $T_{(i)a-Si:H,n}$ seems to result in slightly lower *FF* values despite having denser (i)a-Si:H bilayers (see Figure 3A). This suggests that higher deposition temperatures are not favorable for the passivation and transport of charge carriers, thus resulting in lower V_{OC} and *FF* than samples with (i)a-Si:H deposited at lower temperatures. This observation is also well-aligned with our previous study where nearly 3%_{abs.} *FF* gain was reported by applying the HPTs before the *n*-layer deposition, which improved mainly the V_{OC} of solar cells.³¹ Therefore, as expected, for efficient collections of charge carriers, it is crucial to have (i)a-Si:H layers fostering the passivation quality. Nevertheless, *p*-contact is particularly more sensitive to the bulk quality of (i)a-Si:H

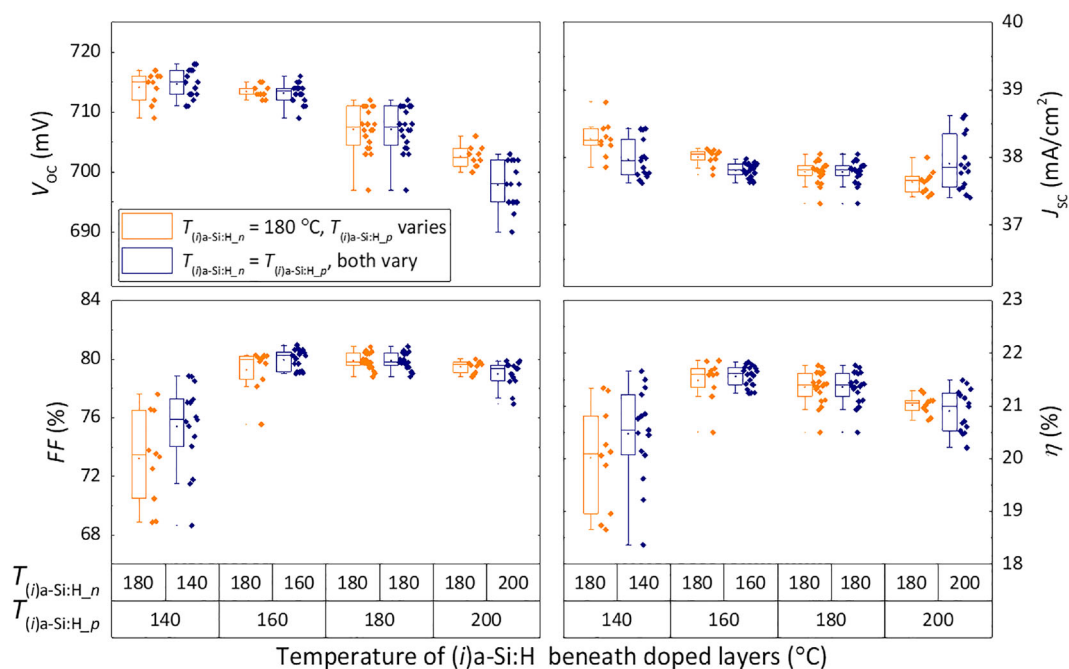


FIGURE 5 The J - V parameters of FBC-SHJ solar cells prepared under various temperatures of $(i)a$ -Si:H bilayers. Solar cells feature both sides screen-printed Ag contacts. Note, $T_{(i)a-Si:H_n}$ and $T_{(i)a-Si:H_p}$ represent the deposition temperature of $(i)a$ -Si:H layer beneath n - and p -layers, respectively. The deposition temperatures of doped layers and HPTs were kept constant at 180°C as listed in Table 2. For the samples that feature $T_{(i)a-Si:H_n} = T_{(i)a-Si:H_p} = 180^\circ\text{C}$, the box plot is duplicated for easier comparison in different temperature series.

TABLE 3 The external parameters of the best FBC-SHJ solar cells in this study. Those cells feature Cu-plated front electrodes and SiO_x /IWO double-layer anti-reflection coating.

$T_{(i)a-Si:H}$ (°C)	V_{OC} (mV)	J_{SC} (mA/cm ²)	FF (%)	η (%)	Certified/in-house measurements
160	724.5	39.81	82.2	23.71	ISFH CalTeC
180	722.1	39.71	82.7	23.71	ISFH CalTeC
160*	726.0	39.97	83.3	24.18	In-house

*This cell features further improved thickness combinations of the p -layer.

layers than n -contact.^{28,29} This observation could be correlated to the different dominant transport mechanisms for collecting electrons (thermionic emission) and holes (tunneling) as also discussed in.^{29,69} Overall, in this study, solar cells with $(i)a$ -Si:H deposited at 160°C exhibited the best efficiencies among all other investigated temperature counterparts owing to their better trade-off between the passivation qualities and the collection of charge carriers.

To exclude any temperature anneal effects during the screen printing (Ag paste curing at 170°C for 40 min), we alternatively applied our optimized room-temperature copper-plating metallization approach³⁴ for cells with $(i)a$ -Si:H deposited under various temperatures and with an additional 100-nm-thick SiO_x capping the front IWO to form a double-layer anti-reflection coating.^{33,35,71} As provided in Figure S4, the J - V parameters of those cells that feature front electroplated Cu electrodes and rear thermally evaporated Ag contacts exhibited similar trends as shown in Figure 5. Noticeably, likely due to the “gentler” process of our optimized copper-plating process,³⁴ the optimum trade-off between V_{OC} and FF was found for the temperature range from 160°C to 180°C. For both $T_{(i)a-Si:H}$ of 160°C to 180°C,

the best cells exhibited an independently certified conversion efficiency of 23.71% (see Table 3 and Figure S5). Based on those results, we improved further the thickness combinations of p -layer of SHJ cells with $(i)a$ -Si:H layers deposited at 160°C, which exhibited a high FF of 83.3%, a V_{OC} of 726.0 mV, a J_{SC} of 39.97 mA/cm², and an efficiency of 24.18% (see Table 3 and Figure S6).

4 | CONCLUSIONS

We studied the effect of $(i)a$ -Si:H deposition temperature on the passivation quality and solar cell performance. Within the investigated temperature range (140°C - 200°C), we observed better passivation qualities of $(i)a$ -Si:H layers deposited under higher temperatures possibly due to their denser film as confirmed by SE and FTIR measurements. Interestingly, porous films deposited under lower temperatures exhibited significantly improved and better passivation qualities with additionally applied HPTs, which favor the formation of porous and H-rich film. Besides, we also noticed distinctive peaks around Si-H W-

RM in the infrared spectra, which seemingly reveal microstructural properties of thin-film (i)a-Si:H layers that are still unclear, for which further investigations on the vibrational origins of those peaks are still required. At the device level, even though we observed the highest V_{OC} s for cells with (i)a-Si:H deposited at the lowest temperature (140°C), the related FFs are poorer as compared to their higher temperature counterparts. The optimal trade-off between V_{OC} and FF was found for SHJ solar cells fabricated with (i)a-Si:H layers deposited from 160°C to 180°C, which exhibited independently certified efficiencies of 23.71%. Further optimized *p*-layers enabled an even higher FF of 83.3% and an efficiency of 24.18% for the cell with (i)a-Si:H deposited at 160°C. As the deposition temperature of (i)a-Si:H and associated materials properties affect solar cells performance, we showed that high performance devices should meet critical requirements in optimizing the (i)a-Si:H that are not only limited to an excellent surface passivation quality to reduce losses induced by interface recombination. Furthermore, (i)a-Si:H films should feature less-defective bulk to not disrupt the collection of charge carriers. We demonstrate that carefully optimizing (i)a-Si:H layers that fulfill both requirements can contribute to higher SHJ solar cell efficiencies.

ACKNOWLEDGEMENTS

This study receives financial support from the NWO Joint Solar Program III (680-91-011) and technical support from PVMD group technicians Martijn Tijssen, Stefaan Heirman, and Daragh O'Connor. The authors thank Dr. Rudi Santbergen from PVMD group for the fruitful discussions about the FTIR study. The authors also acknowledge Dr. Martin Ledinský from the Institute of Physics of the Czech Academy of Sciences for the measurement and discussion on the crystallinity of very thin (*p*)nc-SiO_x:H.

DATA AVAILABILITY STATEMENT

The data that support the findings of this study are available from the corresponding author upon reasonable request.

ORCID

Yifeng Zhao  <https://orcid.org/0000-0003-3789-5090>

Paul Procel  <https://orcid.org/0000-0003-4997-3551>

Can Han  <https://orcid.org/0000-0002-3213-6856>

Liqi Cao  <https://orcid.org/0000-0001-8076-6249>

REFERENCES

- LONGi Solar. LONGi once again sets new world record for HJT solar cell efficiency. 2022.
- CSEM. EPFL and CSEM smash through the 30% efficiency barrier for perovskite-on-silicon-tandem solar cells-setting two certified world records. 2022.
- De Wolf S, Kondo M. Abruptness of a-Si:Hc-Si interface revealed by carrier lifetime measurements. *Appl Phys Lett*. 2007;90(4):1-4.
- Deligiannis D, Vasudevan R, Smets AHM, van Swaaij RA, Zeman M. Surface passivation of c-Si for silicon heterojunction solar cells using high-pressure hydrogen diluted plasmas. *AIP Adv*. 2015;5(9):097165. doi:10.1063/1.4931821
- Zhang Y, Yu C, Yang M, et al. Significant improvement of passivation performance by two-step preparation of amorphous silicon passivation layers in silicon heterojunction solar cells. *Chinese Phys Lett*. 2017;34(3):038101. doi:10.1088/0256-307X/34/3/038101
- Ge J, Ling ZP, Wong J, Mueller T, Aberle G. Optimisation of Intrinsic a-Si:H Passivation Layers in Crystalline-amorphous Silicon Heterojunction Solar Cells. *Energy Procedia*. 2011;2012(15):107-117. doi:10.1016/j.egypro.2012.02.013
- Kim S-K, Lee JC, Park S-J, Kim Y-J, Yoon KH. Effect of hydrogen dilution on intrinsic a-Si: H layer between emitter and Si wafer in silicon heterojunction solar cell. *Sol Energy Mater sol Cells*. 2008;92(3):298-301. doi:10.1016/j.solmat.2007.09.007
- Descroedres A, Barraud L, de Wolf S, et al. Improved amorphous/crystalline silicon interface passivation by hydrogen plasma treatment. *Appl Phys Lett*. 2011;99(12):1-4. doi:10.1063/1.3641899
- Granata SN, Bearda T, Dross F, Gordon I, Poortmans J, Mertens R. Effect of an in-situ H₂ plasma pretreatment on the minority carrier lifetime of a-Si: H (i) passivated crystalline silicon. *Energy Procedia*. 2012;27:412-418. doi:10.1016/j.egypro.2012.07.086
- Zhang L, Guo W, Liu W, et al. Investigation of positive roles of hydrogen plasma treatment for interface passivation based on silicon heterojunction solar cells. *J Phys D Appl Phys*. 2016;49(16):165305. doi:10.1088/0022-3727/49/16/165305
- Soman A, Nsofor U, Das U, Gu T, Hegedus S. Correlation between in situ diagnostics of the hydrogen plasma and the interface passivation quality of hydrogen plasma post-treated a-Si: H in silicon heterojunction solar cells. *ACS Appl Mater Interfaces*. 2019;11(17):16181-16190. doi:10.1021/acsami.9b01686
- Xu M, Wang C, Bearda T, et al. Dry passivation process for silicon heterojunction solar cells using hydrogen plasma treatment followed by in situ a-Si: H deposition. *IEEE J Photovolt*. 2018;8(6):1539-1545. doi:10.1109/JPHOTOV.2018.2871329
- Neumüller A, Sergeev O, Heise SJ, et al. Improved amorphous silicon passivation layer for heterojunction solar cells with post-deposition plasma treatment. *Nano Energy*. 2018;43:228-235. doi:10.1016/j.nanoen.2017.11.053
- Karabanov SM, Reginevich MA. Impact of Hydrogen Plasma Treatment on Intrinsic Amorphous Silicon Bilayers in Silicon Heterojunction Solar Cells. 2021 IEEE Int. Conf. Environ. Electr. Eng. 2021 IEEE Ind. Commer. Power Syst. Eur. (EEEIC/I&CPS Eur. 2021;1-5.
- Zhao Y, Mazzarella L, Procel P, et al. Doped hydrogenated nanocrystalline silicon oxide layers for high-efficiency c-Si heterojunction solar cells. *Prog Photovolt Res Appl*. 2020;28(5):425-435. doi:10.1002/pp.3256
- Lee K-S, Yeon CB, Yun SJ, Jung KH, Lim JW. Improved surface passivation using dual-layered a-Si: H for silicon heterojunction solar cells. *ECS Solid State Lett*. 2014;3(3):P33-P36. doi:10.1149/2.001404ssl
- Sai H, Chen P-W, Hsu H-J, et al. Impact of intrinsic amorphous silicon bilayers in silicon heterojunction solar cells. *J Appl Phys*. 2018;124(10):103102. doi:10.1063/1.5045155
- Bin Mohd Zulkifly FA, Shiratori Y, Nakada K, Miyajima S. Impact of bilayer structures on the surface passivation quality of high-rate-sputtered hydrogenated amorphous silicon for silicon heterojunction solar cells. *Prog Photovolt Res Appl*. 2020;28(9):971-976. doi:10.1002/pp.3298
- Ru X, Qu M, Wang J, et al. 25.11% efficiency silicon heterojunction solar cell with low deposition rate intrinsic amorphous silicon buffer layers. *Sol. Energy Mater. Sol. Cells*. 2020;215:110643. doi:10.1016/j.solmat.2020.110643
- Liu W, Zhang L, Chen R, et al. Underdense a-Si: H film capped by a dense film as the passivation layer of a silicon heterojunction solar cell. *J Appl Phys*. 2016;120(17):175301. doi:10.1063/1.4966941
- Sai H, Hsu H-J, Chen P-W, Chen P-L, Matsui T. Intrinsic amorphous silicon bilayers for effective surface passivation in silicon heterojunction solar cells: a comparative study of interfacial layers. *Phys. Status Solidi*. 2021;218(9):2000743. doi:10.1002/pssa.202000743

22. Qu X, He Y, Qu M, et al. Identification of embedded nanotwins at c-Si/a-Si:H interface limiting the performance of high-efficiency silicon heterojunction solar cells. *Nat Energy*. 2021;6(2):1-9. doi:[10.1038/s41560-020-00768-4](https://doi.org/10.1038/s41560-020-00768-4)
23. Dauwe S, Schmidt J, Hezel R. Very low surface recombination velocities on p-and n-type silicon wafers passivated with hydrogenated amorphous silicon films. *Conf Rec Twenty-Ninth IEEE Photovolt Spec Conf*. 2002;2002:1246-1249.
24. Macco B, Melskens J, Podraza NJ, et al. Correlating the silicon surface passivation to the nanostructure of low-temperature a-Si: H after rapid thermal annealing. *J Appl Phys*. 2017;122(3):035302. doi:[10.1063/1.4994795](https://doi.org/10.1063/1.4994795)
25. De Wolf S, Kondo M. Boron-doped a-Si:H/c-Si interface passivation: degradation mechanism. *Appl Phys Lett*. 2007;91(11):112109. doi:[10.1063/1.2783972](https://doi.org/10.1063/1.2783972)
26. Demareux B, De Wolf S, Descoeudres A, Charles Holman Z, Ballif C. Damage at hydrogenated amorphous/crystalline silicon interfaces by indium tin oxide overlayer sputtering. *Appl Phys Lett*. 2012;101(17):1-5. doi:[10.1063/1.4764529](https://doi.org/10.1063/1.4764529)
27. Procel P, Yang G, Isabella O, Zeman M. Theoretical evaluation of contact stack for high efficiency IBC-SHJ solar cells. *Sol Energy Mater Sol Cells*. 2018;186:66-77. doi:[10.1016/j.solmat.2018.06.021](https://doi.org/10.1016/j.solmat.2018.06.021)
28. Wu Z, Zhang L, Liu W, et al. Role of hydrogen in modifying a-Si: H/c-Si interface passivation and band alignment for rear-emitter silicon heterojunction solar cells. *J Mater Sci Mater Electron*. 2020;31(12):9468-9474. doi:[10.1007/s10854-020-03486-5](https://doi.org/10.1007/s10854-020-03486-5)
29. Luderer C, Kurt D, Moldovan A, Hermle M, Bivour M. Intrinsic layer modification in silicon heterojunctions: balancing transport and surface passivation. *Sol. Energy Mater. Sol. Cells*. 2022;238:111412. doi:[10.1016/j.solmat.2021.111412](https://doi.org/10.1016/j.solmat.2021.111412)
30. Zhao Y, Procel P, Han C, et al. Design and optimization of hole collectors based on nc-SiO_x: H for high-efficiency silicon heterojunction solar cells. *Sol Energy Mater Sol Cells*. 2021;219:110779. doi:[10.1016/j.solmat.2020.110779](https://doi.org/10.1016/j.solmat.2020.110779)
31. Zhao Y, Mazzarella L, Procel P, et al. Ultra-thin electron collectors based on nc-Si: H for high-efficiency silicon heterojunction solar cells. *Prog Photovolt Res Appl*. 2022;30(8):809-822. doi:[10.1002/ppp.3502](https://doi.org/10.1002/ppp.3502)
32. Yang G, Guo P, Procel P, et al. High-efficiency black IBC c-Si solar cells with poly-Si as carrier-selective passivating contacts. *Sol Energy Mater Sol Cells*. 2018;186:9-13. doi:[10.1016/j.solmat.2018.06.019](https://doi.org/10.1016/j.solmat.2018.06.019)
33. Han C, Zhao Y, Mazzarella L, et al. Room-temperature sputtered tungsten-doped indium oxide for improved current in silicon heterojunction solar cells. *Sol. Energy Mater. Sol. Cells*. 2021;227:111082. doi:[10.1016/j.solmat.2021.111082](https://doi.org/10.1016/j.solmat.2021.111082)
34. Han C, Yang G, Procel P, et al. Controllable simultaneous bifacial Cu-plating for high efficiency crystalline silicon solar cells. *Sol RRL*. 2022; (6):2100810. doi:[10.1002/solr.202100810](https://doi.org/10.1002/solr.202100810)
35. Zhang D, Digdaya IA, Santbergen R, et al. Design and fabrication of a SiO_x/ITO double-layer anti-reflective coating for heterojunction silicon solar cells. *Sol. Energy Mater. Sol. Cells*. 2013;117:132-138. doi:[10.1016/j.solmat.2013.05.044](https://doi.org/10.1016/j.solmat.2013.05.044)
36. Pysch D, Mette A, Glunz SW. A review and comparison of different methods to determine the series resistance of solar cells. *Sol Energy Mater sol Cells*. 2007;91(18):1698-1706. doi:[10.1016/j.solmat.2007.05.026](https://doi.org/10.1016/j.solmat.2007.05.026)
37. Bhattacharya E, Mahan AH. Microstructure and the light-induced metastability in hydrogenated amorphous silicon. *Appl Phys Lett*. 1988;52(19):1587-1589. doi:[10.1063/1.99089](https://doi.org/10.1063/1.99089)
38. Brodsky MH, Cardona M, Cuomo JJ. Infrared and Raman spectra of the silicon-hydrogen bonds in amorphous silicon prepared by glow discharge and sputtering. *Phys. Rev. B*. 1977;16(8):3556-3571. doi:[10.1103/PhysRevB.16.3556](https://doi.org/10.1103/PhysRevB.16.3556)
39. Langford AA, Fleet ML, Nelson BP, Lanford WA, Maley N. Infrared absorption strength and hydrogen content of hydrogenated amorphous silicon. *Phys. Rev. B*. 1992;45(23):13367. doi:[10.1103/PhysRevB.45.13367](https://doi.org/10.1103/PhysRevB.45.13367)
40. Smets AHM, Kessels WMM, Van de Sanden MCM. Vacancies and voids in hydrogenated amorphous silicon. *Appl Phys Lett*. 2003; 82(10):1547-1549. doi:[10.1063/1.1559657](https://doi.org/10.1063/1.1559657)
41. Schulze TF, Korte L, Ruske F, Rech B. Band lineup in amorphous/crystalline silicon heterojunctions and the impact of hydrogen microstructure and topological disorder. *Phys. Rev. B*. 2011; 83(16):165314. doi:[10.1103/PhysRevB.83.165314](https://doi.org/10.1103/PhysRevB.83.165314)
42. Nunomura S, Sakata I, Sakakita H, Koga K, Shiratani M. Real-time monitoring of surface passivation of crystalline silicon during growth of amorphous and epitaxial silicon layer. *J Appl Phys*. 2020;128(3): 033302. doi:[10.1063/5.0011563](https://doi.org/10.1063/5.0011563)
43. Lucovsky G, Nemanich RJ, Knights JC. Structural interpretation of the vibrational spectra of a-Si: H alloys. *Phys Rev B*. 1979;19(4):2064-2073. doi:[10.1103/PhysRevB.19.2064](https://doi.org/10.1103/PhysRevB.19.2064)
44. Beyer W, Ghazala MSA. Absorption strengths of Si-H vibrational modes in hydrogenated silicon. *MRS Online Proc Libr Arch*. 1998;507. doi:[10.1557/PROC-507-601](https://doi.org/10.1557/PROC-507-601)
45. Mahan AH, Williamson DL, Nelson BP, Crandall RS. Small-angle X-ray scattering studies of microvoids in a-SiC: H and a-Si: H. *Sol Cells*. 1989;27(1-4):465-476. doi:[10.1016/0379-6787\(89\)90056-2](https://doi.org/10.1016/0379-6787(89)90056-2)
46. Gotoh K, Wilde M, Kato S, et al. Hydrogen concentration at a-Si: H/c-Si heterointerfaces—the impact of deposition temperature on passivation performance. *AIP Adv*. 2019;9(7):075115. doi:[10.1063/1.5100086](https://doi.org/10.1063/1.5100086)
47. Schulze TF, Beushausen HN, Leendertz C, Dobrich A, Rech B, Korte L. Interplay of amorphous silicon disorder and hydrogen content with interface defects in amorphous/crystalline silicon heterojunctions. *Appl Phys Lett*. 2010;96(25):252102. doi:[10.1063/1.3455900](https://doi.org/10.1063/1.3455900)
48. Smets AHM, Van De Sanden MCM. Relation of the Si a H stretching frequency to the nanostructural Si a H bulk environment. *Phys Rev B*. 2007;76:1-4.
49. Burrows MZ, Das UK, Opila RL, De Wolf S, Birkmire RW. Role of hydrogen bonding environment in a-Si:H films for c-Si surface passivation. *J Vac Sci Technol A Vac Surf Film*. 2008;26(4):683-687. doi:[10.1116/1.2897929](https://doi.org/10.1116/1.2897929)
50. Smakula A. Über erregung und entfärbung lichtelektrisch leitender alkali-halogenide. *Zeitschrift Phys*. 1930;59(9):603-614. doi:[10.1007/BF01344801](https://doi.org/10.1007/BF01344801)
51. Shanks H, Fang CJ, Ley L, Cardona M, Demond FJ, Kalbitzer S. Infrared spectrum and structure of hydrogenated amorphous silicon. *Phys Status Solidi*. 1980;100(1):43-56. doi:[10.1002/pssb.2221000103](https://doi.org/10.1002/pssb.2221000103)
52. Maley N. Critical investigation of the infrared-transmission-data analysis of hydrogenated amorphous silicon alloys. *Phys. Rev. B*. 1992; 46(4):2078-2085. doi:[10.1103/PhysRevB.46.2078](https://doi.org/10.1103/PhysRevB.46.2078)
53. Manfredotti C, Fizzotti F, Boero M, Pastorino P, Polesello P, Vittone E. Influence of hydrogen-bonding configurations on the physical properties of hydrogenated amorphous silicon. *Phys. Rev. B*. 1994;50(24):18046. doi:[10.1103/PhysRevB.50.18046](https://doi.org/10.1103/PhysRevB.50.18046)
54. Fang CJ, Gruntz KJ, Ley L, et al. The hydrogen content of a-Ge: H and a-Si: H as determined by IR spectroscopy, gas evolution and nuclear reaction techniques. *J Non Cryst Solids*. 1980;35:255-260. doi:[10.1016/0022-3093\(80\)90603-1](https://doi.org/10.1016/0022-3093(80)90603-1)
55. Cardona M. Vibrational spectra of hydrogen in silicon and germanium. *Phys Status Solidi B, Basic Res*. 1983;118(2):463-481. doi:[10.1002/pssb.2221180202](https://doi.org/10.1002/pssb.2221180202)
56. Xu Y, Liao X, Kong G, et al. Microstructure characterization of transition films from amorphous to nanocrystalline silicon. *J Cryst Growth*. 2003;256(1-2):27-32. doi:[10.1016/S0022-0248\(03\)01342-3](https://doi.org/10.1016/S0022-0248(03)01342-3)
57. Hou G-F, Geng X-H, Zhang X-D, Sun J, Zhang JJ, Zhao Y. Evolution of infrared spectra and optical emission spectra in hydrogenated silicon thin films prepared by VHF-PECVD. *Chinese Phys B*. 2011;20(7): 077802. doi:[10.1088/1674-1056/20/7/077802](https://doi.org/10.1088/1674-1056/20/7/077802)

58. Robertson J. Deposition mechanism of hydrogenated amorphous silicon. *J Appl Phys*. 2000;87(5):2608-2617. doi:[10.1063/1.372226](https://doi.org/10.1063/1.372226)
59. Fujiwara H, Toyoshima Y, Kondo M, Matsuda A. Interface-layer formation mechanism in a-Si:H thin-film growth studied by real-time spectroscopic ellipsometry and infrared spectroscopy. *Phys. Rev. B*. 1999;60(19):13598. doi:[10.1103/PhysRevB.60.13598](https://doi.org/10.1103/PhysRevB.60.13598)
60. Fujiwara H, Kondo M, Matsuda A. Depth profiling of silicon-hydrogen bonding modes in amorphous and microcrystalline Si: H thin films by real-time infrared spectroscopy and spectroscopic ellipsometry. *J Appl Phys*. 2002;91(7):4181-4190. doi:[10.1063/1.1457535](https://doi.org/10.1063/1.1457535)
61. Geissbühler J, de Wolf S, Demareux B, et al. Amorphous/crystalline silicon interface defects induced by hydrogen plasma treatments. *Appl Phys Lett*. 2013;102(23):231604. doi:[10.1063/1.4811253](https://doi.org/10.1063/1.4811253)
62. Street RA, Tsai CC, Kakalios J, Jackson WB. Hydrogen diffusion in amorphous silicon. *Philos Mag B*. 1987;56(3):305-320. doi:[10.1080/13642818708221319](https://doi.org/10.1080/13642818708221319)
63. Street RA. Hydrogen diffusion and electronic metastability in amorphous silicon. *Phys B Condens Matter*. 1991;170(1-4):69-81. doi:[10.1016/0921-4526\(91\)90108-Q](https://doi.org/10.1016/0921-4526(91)90108-Q)
64. Beyer W. Hydrogen effusion: a probe for surface desorption and diffusion. *Phys B Condens Matter*. 1991;170(1-4):105-114. doi:[10.1016/0921-4526\(91\)90111-Q](https://doi.org/10.1016/0921-4526(91)90111-Q)
65. De Wolf S, Kondo M. Surface passivation properties of stacked doped PECVD a-Si: H layers for hetero-structure c-Si solar cells. 2006 IEEE 4th world Conf. Photovolt Energy Conf 2006;2: 1469-1472.
66. Roca i Cabarrocas P, Layadi N, Drevillon B, Solomon I. Microcrystalline silicon growth by the layer-by-layer technique: long term evolution and nucleation mechanisms. *J Non Cryst Solids*. 1996;198-200: 871-874.
67. Layadi N, Roca i Cabarrocas P, Drévillon B, Solomon I. Real-time spectroscopic ellipsometry study of the growth of amorphous and microcrystalline silicon thin films prepared by alternating silicon deposition and hydrogen plasma treatment. *Phys Rev B*. 1995;52(7):5136-5143. doi:[10.1103/PhysRevB.52.5136](https://doi.org/10.1103/PhysRevB.52.5136)
68. Matsuda A. Formation kinetics and control of microcrystallite in $\mu\text{c-Si:H}$ from glow discharge plasma. *J Non Cryst Solids*. 1983;59-60:767-774. doi:[10.1016/0022-3093\(83\)90284-3](https://doi.org/10.1016/0022-3093(83)90284-3)
69. Procel P, Xu H, Saez A, et al. The role of heterointerfaces and subgap energy states on transport mechanisms in silicon heterojunction solar cells. *Prog Photovolt Res Appl*. 2020;28(9):935-945. doi:[10.1002/pip.3300](https://doi.org/10.1002/pip.3300)
70. Adachi D, Hernández JL, Yamamoto K. Impact of carrier recombination on fill factor for large area heterojunction crystalline silicon solar cell with 25.1% efficiency. *Appl Phys Lett*. 2015;107(23):233506. doi:[10.1063/1.4937224](https://doi.org/10.1063/1.4937224)
71. Han C, Santbergen R, van Duffelen M, et al. Towards bifacial silicon heterojunction solar cells with reduced TCO use. *Prog Photovoltaics Res Appl*. 2022;30(7):750-762. doi:[10.1002/pip.3550](https://doi.org/10.1002/pip.3550)

SUPPORTING INFORMATION

Additional supporting information can be found online in the Supporting Information section at the end of this article.

How to cite this article: Zhao Y, Procel P, Smets A, et al. Effects of (i)a-Si:H deposition temperature on high-efficiency silicon heterojunction solar cells. *Prog Photovolt Res Appl*. 2023;31(12):1170-1180. doi:[10.1002/pip.3620](https://doi.org/10.1002/pip.3620)